Comprehensive optical characterization of atomically thin NbSe_{2}

Heather M. Hill, Albert F. Rigosi, Sergiy Krylyuk, Jifa Tian, Nhan V. Nguyen, Albert V. Davydov, David B. Newell, and Angela R. Hight Walker

Phys. Rev. B **98**, 165109 — Published 5 October 2018

DOI: 10.1103/PhysRevB.98.165109

Comprehensive optical characterization of atomically thin $NbSe_2$

Heather M. Hill[1], Albert F. Rigosi[1*], Sergiy Krylyuk[2,3], Jifa Tian[1,4], Nhan V. Nguyen[1], Albert V. Davydov[2], David B. Newell[1], and Angela R. Hight Walker[1]

[1]*Physical Measurement Laboratory, National Institute of Standards and Technology (NIST), Gaithersburg, MD 20899, United States*

[2]*Material Measurement Laboratory, National Institute of Standards and Technology (NIST), Gaithersburg, MD 20899, United States*

[3]*Theiss Research, Inc., La Jolla, CA 92037, United States*

[4]*Department of Physics and Astronomy, and Birck Nanotechnology Center, Purdue University, West Lafayette, Indiana 47907, United States*

(Received 10 August 2018;)

ABSTRACT: Transition metal dichalcogenides (TMDCs) have offered experimental access to quantum confinement in one dimension. In recent years, metallic TMDCs like $NbSe_2$ have taken center stage with many of them exhibiting interesting temperature-dependent properties such as charge density waves and superconductivity. In this work, we perform a comprehensive optical analysis of $NbSe_2$ by utilizing Raman spectroscopy, differential reflectance contrast, and spectroscopic ellipsometry. These analyses, when coupled with Kramers-Kronig analysis, allow us to extract the dielectric functions of bulk and atomically thin $NbSe_2$ and relate them to the resonant behavior of the Raman spectra.

PACS numbers: 78.30.Er, 74.25.nd, 73.40.-q, 77.22.Ch

* Email: albert.rigosi@nist.gov; +1-301-975-6572

I. INTRODUCTION

Transition metal dichalcogenides (TMDCs) are a class of materials, which when reduced to two dimensions, yield a lot of fascinating properties, including, but not limited to, the exhibition of a direct bandgap [1-7] and distinct many-body effects [8-10]. Moreover, these materials have extensive applicability in the advancement of optoelectronics, photovoltaics, spintronics, energy storage, and biophysical systems [11-14]. Metallic TMDCs, such as $NbSe_2$, exhibit properties such as the charge density wave (CDW) states [15-22], superconductivity [23-27], and other quantum phenomena that persist in the monolayer limit [28-31]. $NbSe_2$ has been studied by various non-optical methods [32-36], as well as optical in the case of bulk $NbSe_2$ [37]. While there have been a number of optical investigations of bulk $NbSe_2$ for obtaining Raman spectra [38] and optical constants [39-40], there are only few works that provide a more comprehensive review of the optical properties as the thickness is decreased to a monolayer [41-45]. Furthermore, research on the dielectric function of atomically thin $NbSe_2$ is limited [46].

In this work, detailed optical spectroscopies were utilized to complete a thorough examination of atomically thin flakes exfoliated from $NbSe_2$ crystals grown using the chemical vapor transport (CVT) method. Raman spectra were acquired over a large parameter space, including layer number, excitation wavelength, and temperature. Specifically, flakes were characterized with traditional [47-49] and resonance [50-56] Raman spectroscopy and verified to be superconducting by measuring electrical transport. To further characterize thin $NbSe_2$ we used differential reflectance contrast (DRC), which reveals both the reflectivity of the material and, when paired with Kramers-Kronig analysis (KKA), the dielectric function $\varepsilon(E)$ as a function of energy. As an accompanying technique to DRC, spectroscopic ellipsometry (SE) was also used to directly confirm $\varepsilon(E)$ for bulk $NbSe_2$, substantiating the validity of using KKA to extract the

dielectric function of mono- to few-layer $NbSe_2$ for photon energies in the visible range (between 1.15 eV to 3.5 eV).

II. EXPERIMENTAL METHODS

A. Crystal Growth and Sample Preparation

Centimeter-sized $NbSe_2$ single-crystals were grown using the iodine-assisted CVT method. Polycrystalline $NbSe_2$ powders were synthesized by reacting stoichiometric amounts of Nb (99.9 %, Strem Chemicals) and Se (99.999 %, Strem Chemicals) [57] powders in vacuum-sealed quartz ampoule at 850 °C for 3 days. Next, quartz ampoules containing less than 1.5 g of $NbSe_2$ charge and less than 80 mg (3.7 mg/cm^3) of I_2 transport agent were sealed under vacuum and placed in a single-zone furnace. Temperature at the charge and growth zones were between 825 °C and 700 °C and the growth duration was 140 h. $NbSe_2$ crystals were mechanically exfoliated onto silicone elastomer polydimethylsiloxane (PDMS) and then transferred onto both Si/SiO_2 (oxide thickness of 300 nm) and fused quartz substrates.

B. Traditional and Resonance Raman Spectroscopy

Traditional and resonance Raman spectroscopy was performed on bulk (approximately 50 nm) and thin (4 layers or fewer) $NbSe_2$ in an inert gas environment as a function of temperature, excitation wavelength, and polarization. For the latter, the polarization of the incoming light was kept fixed while the parallel and cross components of the response were measured separately. The flake thickness was verified using the energy of the Raman shear mode and E_{2g} mode [21, 43]. Raman spectra were collected by a Horiba T64000 triple-grating spectrometer [57] and measured at temperatures from 300 K to 4 K. Discrete excitation lines from the following lasers:

argon ion, helium neon, and tunable dye, including, but not limited to, 476.2 nm, 632.8 nm, 514 nm, and 570 nm were used with powers ranging from 1 μW to 500 μW and spot sizes of about 1 μm. Acquisition times varied between 10 min and 30 min.

C. Differential Reflectance Contrast Spectroscopy

Another optical technique used was DRC, which involves probing a sample of interest by a combined broadband emission from a halogen lamp with a spot size of approximately 10 μm. The optical responses of mono- to few-layer $NbSe_2$ were characterized from the DRC spectra, which are labelled as $\frac{\Delta R}{R}$. Here, $\frac{\Delta R}{R} = \frac{R_{NbSe2} - R_{quartz}}{R_{quartz}}$, where R_{NbSe2} is the reflectance of the flake on top of the fused quartz substrate, and R_{quartz} denotes the reflectance of the bare fused quartz substrate. The reflected light was collected by a spectrometer. To inhibit the effects of oxidation, flakes were exfoliated and immediately measured in ambient conditions at room temperature over a wavelength range of 350 nm to 1080 nm (photon energies of 1.15 eV to 3.5 eV) with 0.75 nm resolution.

D. Spectroscopic Ellipsometry

SE measurements were performed with a Woollam M-2000 Ellipsometer [57] covering a wavelength range from about 145 nm to 1240 nm (1.24 eV to 5.88 eV) with 1.25 nm resolution. The elliptical spot size measured approximately 100 μm along the semi-minor axis and 200 μm to 300 μm along the semi-major axis. SE is a measurement of the change in phase and polarization state of the light reflected from $NbSe_2$. Only bulk material was used to directly extract $\varepsilon(E)$. Data was acquired at two angles of incidence (60° and 70°) and was converted by the software from Fresnel reflection coefficients representative of *p* and *s* polarized light (R_p and

R_s) to the related quantities psi and delta (Ψ and Δ), where $\frac{R_p}{R_s} = e^{i\Delta} \tan \Psi$. The dielectric function of the $NbSe_2$ was then converted from psi and delta directly. The advantage of SE is that it can be used to complement DRC measurements for verifying a material's dielectric behavior by using the WVASE32 modeling program [57].

III. RAMAN CHARACTERIZATION OF SUPERCONDUCTING NIOBIUM DISELENIDE

Figure 1 (a) shows an illustration of the crystal structure of monolayer 2H-$NbSe_2$, with an accompanying optical image shown in (b). The Raman spectra of the A_{1g} and E_{2g} modes for the CVT-grown crystal, taken with a 514 nm laser, are summarized in Figure 1 (c) for bulk, trilayer (3L), bilayer (2L), and monolayer (1L) $NbSe_2$. The soft Raman mode, or the second-order scattering process of two phonons, is also shown. In all spectra, the A_{1g}, E_{2g}, and soft Raman modes were fit with Lorentzian peaks to extract the Raman shift, FWHM, and integrated intensity. The bulk A_{1g}, E_{2g}, and soft modes are centered approximately at 230 cm^{-1}, 240 cm^{-1}, and 180 cm^{-1}, respectively, and in agreement with the literature [21, 46, 55, 58]. The A_{1g} and E_{2g} modes diverge in Figure 1 (d), with the E_{2g} shifting more strongly, as the layer number is reduced to 1L [43].

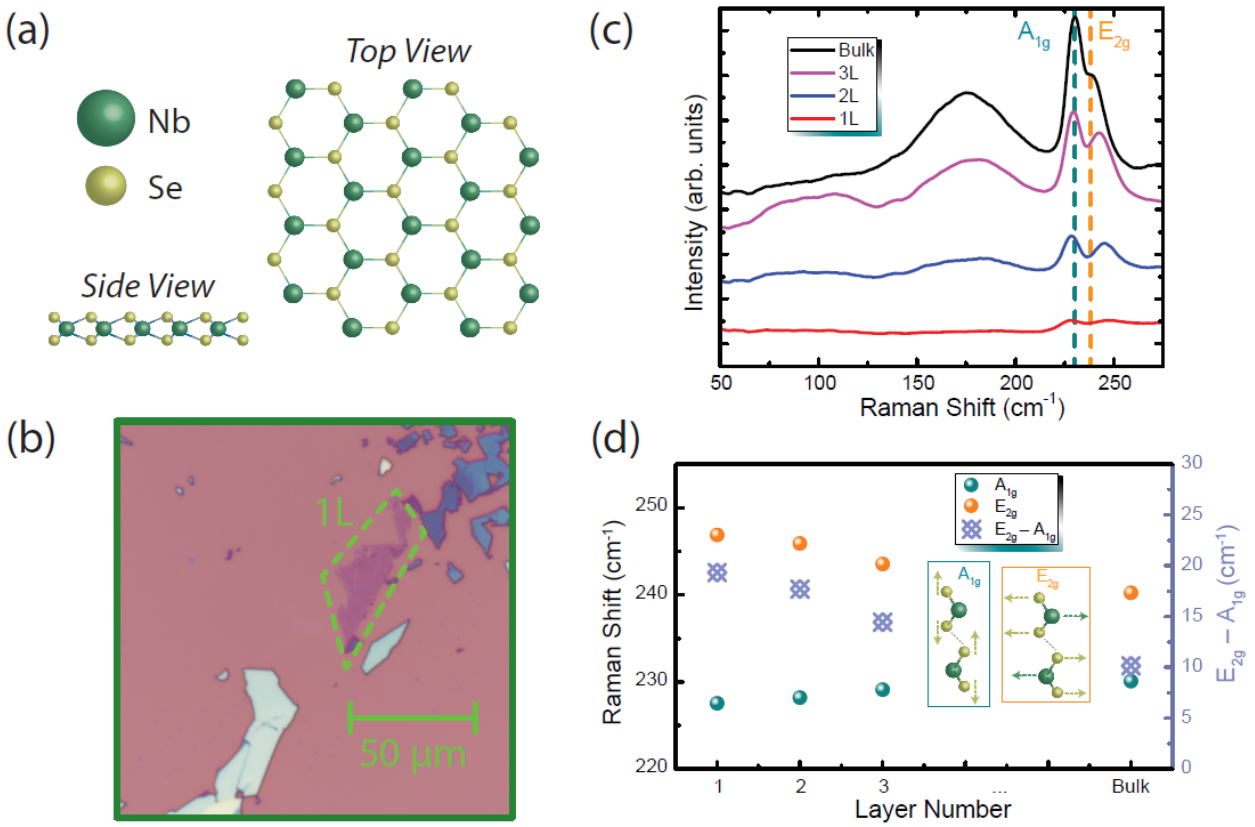

FIG. 1. (Color online) (a) An illustration of the crystal structure of monolayer 2H-$NbSe_2$, along with (b) an optical image of an example flake mechanically exfoliated onto Si/SiO_2. The area containing the monolayer (1L) flake is enclosed by a dashed green line. (c) Raman results for 1L, 2L, 3L, and bulk $NbSe_2$ for an excitation wavelength of 514 nm. The dashed dark cyan and orange lines are meant to guide the eye to the bulk A_{1g} and E_{2g} modes, respectively. (d) The positions of the A_{1g} and E_{2g} modes are plotted as a function of layer number (left vertical axis) with dark cyan and orange points, respectively. The separation of the two modes (labelled on the right vertical axis) is shown with a set of crosses. The inserts are visualizations of the mode vibrations.

To further explore the Raman behavior of $NbSe_2$, spectra were measured as a function of excitation wavelength for cross and parallel polarizations (see the Supplemental Material) [59]. The frequency, FWHM, and relative intensities of the Raman peaks were monitored as the laser was changed. All flakes thicknesses were measured at three wavelengths or more (with 476 nm, 514 nm, and 633 nm) with bulk being measured at additional wavelengths.

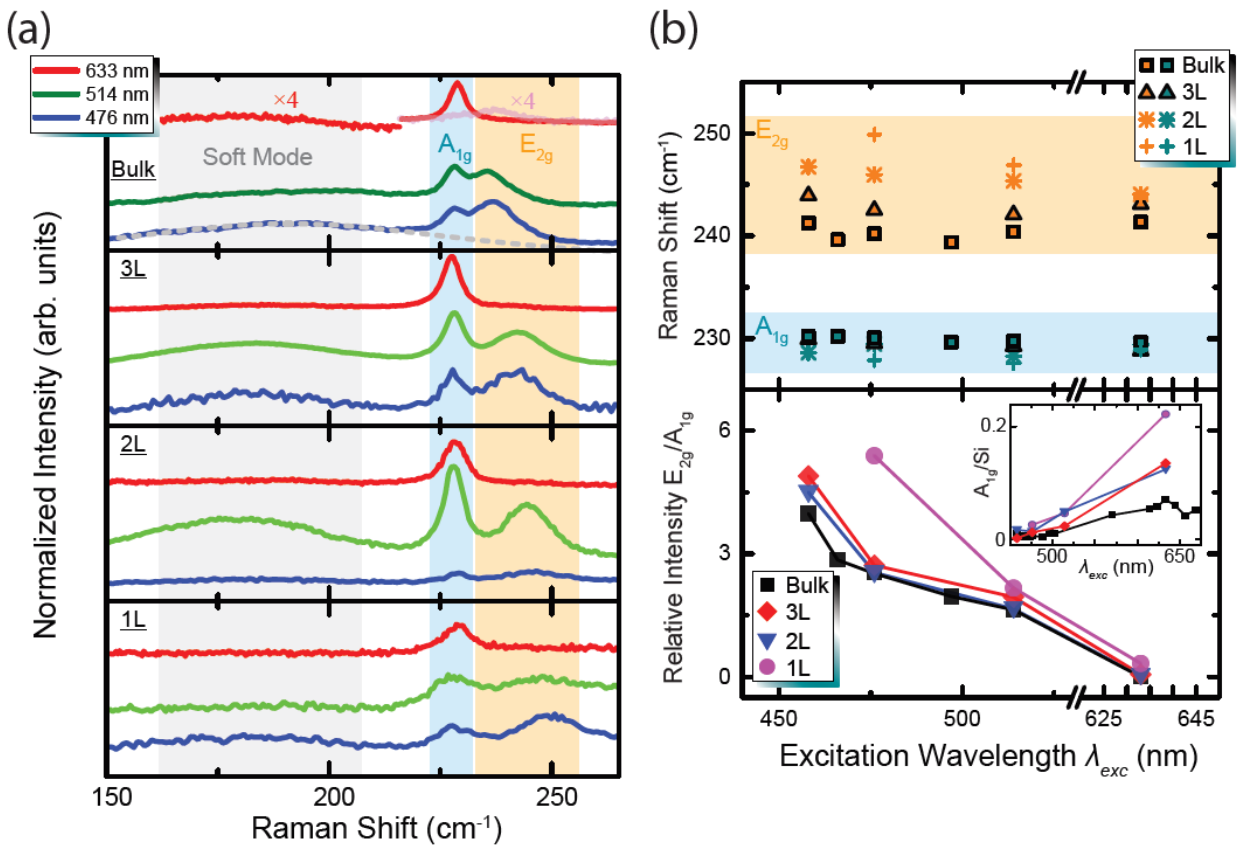

FIG. 2. (Color online) (a) Raman spectra are acquired for several wavelengths for 1L, 2L, 3L, and bulk $NbSe_2$. The gray, blue, and orange bands highlight regions where the soft mode, A_{1g}, and E_{2g} modes are observed, respectively. For the case of bulk, the soft mode and the E_{2g} mode are amplified by a factor of four for clarity in the 633 nm spectrum. (b) The resonance Raman data are summarized by their peak positions in the top panel, with the blue and orange bands still indicating the A_{1g} and E_{2g} modes, respectively. The bottom panel shows the relative intensities of E_{2g}/A_{1g}, with the inset showing the relative intensity of the A_{1g} with respect to the silicon peak as measured through the oxide layer.

Figure 2 (a) shows the Raman spectra obtained with three wavelengths and for varying flake thickness. Three regions of interest are highlighted using gray, blue, and orange bands for the soft mode, A_{1g}, and E_{2g} modes, respectively. An example soft mode fitting is shown in the bulk case at 476 nm. For the 633 nm spectrum, both the soft mode and the E_{2g} mode are multiplied by a factor of four for clarity. In cross polarized measurements, the A_{1g} mode is not observed

allowing the E_{2g} mode to be readily observed even when its intensity is weak. More details on the soft mode are provided in the Supplemental Material [59].

To better view the overall behavior of the A_{1g} and E_{2g} modes, both their peak positions and relative intensities are shown as a function of wavelength in Figure 2 (b). The same blue and orange bands are used to highlight the modes' behavior with layer number and wavelength. With the resonance Raman data in Fig. 2 (b), we find that the E_{2g} Raman mode has a significantly higher intensity relative to the A_{1g} when excited with shorter wavelengths and that the A_{1g} has increasing relative intensity with longer wavelengths which does not align with the scaling of the Raman scattering strength with wavelength (λ^{-4}). One possible reason for this phenomenon will be addressed at the end of the next section.

Next, temperature-dependent Raman measurements were performed on bulk $NbSe_2$ as well as resonance measurements performed at 4K. Figure 3 (a) shows the resonance Raman data taken at 4 K, which yields the same relative intensity trends as the room temperature data. Representative temperature-dependent spectra are shown in Figure 3 (b) at an excitation wavelength of 514 nm. The full temperature-dependent data are summarized in Figure 3 (c) and include the Raman shift, FWHM, and normalized intensity for two wavelengths. When evaluating the behavior of the A_{1g} and E_{2g} modes with decreasing temperature, one can make three observations.

The first trend is an asymptotic redshift of the Raman frequencies with decreasing temperature. The redshift is more pronounced for the E_{2g} mode than the A_{1g}, and those same redshifts are larger for 476 nm than for 514 nm. For the FWHM of the modes, only the E_{2g} mode demonstrates significant narrowing with decreasing temperature, while the change in excitation wavelength produces a negligible effect on the width. Lastly, and more importantly, the

normalized intensity for both modes generally increases as the temperature decreases. However, the difference in the intensity trend between the two excitation wavelengths is substantial for temperatures above about 30 K with the intensity decreasing much more significantly when excited with 514 nm. One possible reason for this difference could be attributed to the bulk transition at 33 K [47], under which an electron quantum fluid, or charge density wave state, forms.

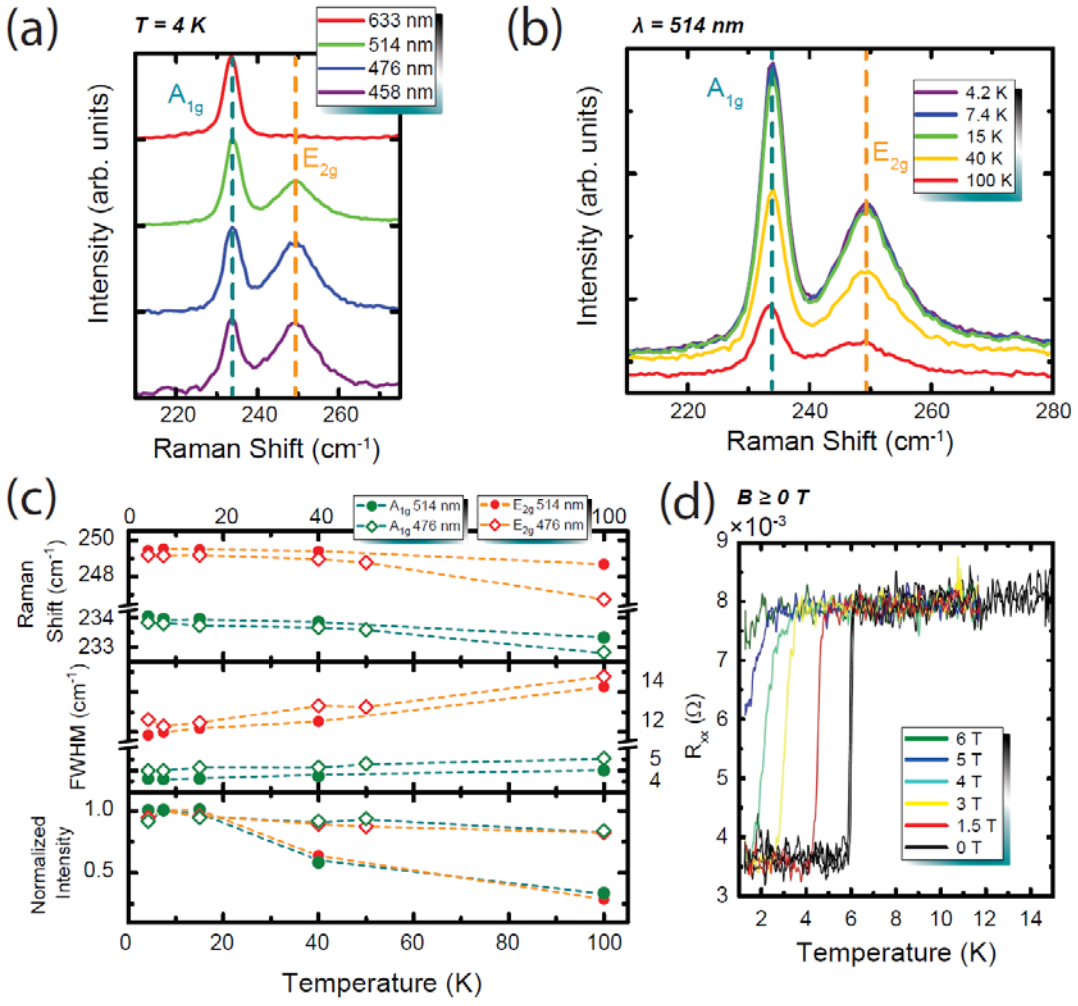

FIG. 3. (Color online) (a) The Raman spectra of bulk $NbSe_2$ acquired at 4 K for four different wavelengths. In this figure, all dashed dark cyan and orange lines indicate the A_{1g} and E_{2g} modes, respectively. (b) Raman spectra as a function of temperature for 514 nm excitation. (c) Raman peak positions, FWHMs, and normalized intensities plotted for two wavelengths

(indicated by different symbols) as a function of temperature. (d) Resistance of a bulk $NbSe_2$ device plotted as a function of temperature, with different color curves representing different magnetic field values.

Finally, we performed temperature-dependent electronic transport measurements, shown in Figure 3 (d). The bulk resistance was measured as a function of temperature with different applied out-of-plane magnetic fields, and, as expected for a superconducting material, a discontinuous drop occurs at the transition temperature of about 6.1 K.

IV. REFLECTANCE ANALYSIS AND THE DIELECTRIC FUNCTION

A. DRC and SE Measurements

Additional optical properties can be measured with both SE and DRC, offering a more comprehensive optical description of thin $NbSe_2$. Figure 4 (a) shows the data obtained with DRC. Bulk, 3L, 2L, and 1L flakes were measured on fused quartz to more easily prepare the data for KKA. Specifically, when the thin material is on a transparent substrate, the DRC data is approximately proportional to the absorption (A) of the material [60-63]. The absorption is predominantly determined by the imaginary component of the dielectric function (ε_2), and thus, gives one a starting point to estimate ε_2, with the dielectric function assuming the form $\varepsilon(E) = \varepsilon_1(E) + i\varepsilon_2(E)$. The approximate relation between the DRC and absorption is given in Equation 1, where n_q is the index of refraction of fused quartz, valued at 1.46.

$$\frac{\Delta R}{R} \approx \frac{4}{n_q^2 - 1} A \tag{1}$$

The goal is to compare $\varepsilon_{bulk}(E)$ obtained directly with SE to the same quantity obtained using DRC and KKA. A favorable comparison in bulk will support the use of the KKA for determining

the dielectric function of mono- to few-layer $NbSe_2$ where SE measurements are not possible due to sample size. Measurements were done on freshly cleaved bulk material to prevent oxidation effects (see Supplemental Material) [59]. The KKA results will be presented in the next subsection. One of the benefits of performing SE on a bulk material is two-fold: (1) the thickness does not need to be known to within a nanometer since the optical constants don't change with perturbations to bulk thickness, and (2) all incoming light only interacts with the bulk. In other cases, light interacting with multiple thin layers having different properties would render the data a representation of a hybrid material. In other words, the so-called pseudo-dielectric function would be generated, requiring careful layer-by-layer analysis to extract the correct dielectric function for each of the constituent material layers. However, in our case, the output SE data does not hybridize the bulk with the quartz beneath.

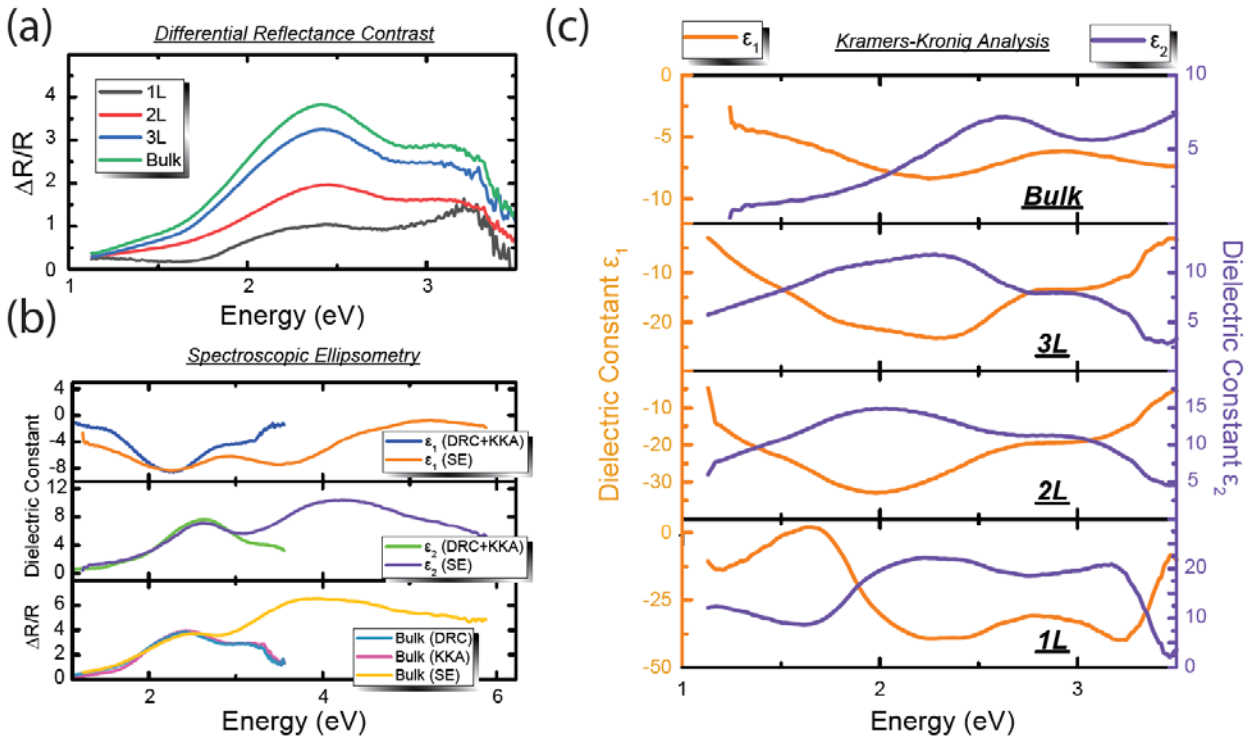

FIG. 4. (Color online) (a) The DRC spectra for bulk and thin $NbSe_2$ is shown. These spectra are converted into absorption to obtain an initial guess for ε_2. (b) In the case of bulk $NbSe_2$, its DRC spectrum is converted and undergoes KKA, with the resulting $\varepsilon_{\text{bulk}}(E)$ shown in the top and middle panels as their real (blue) and imaginary (green) components, respectively. This result is compared with the direct measurement of $\varepsilon_{\text{bulk}}(E)$ by SE, whose real and imaginary components are also in the top (orange curve) and middle (purple curve) panels, respectively. The bottom panel shows the original bulk DRC spectrum (light blue), as well as two generated DRC curves. The pink and yellow curves are obtained when regenerating a DRC spectrum with the KKA-extracted and SE-extracted dielectric functions, respectively. (c) The KKA-extracted dielectric functions are shown for bulk, 3L, 2L, and 1L $NbSe_2$. The real and imaginary components are represented by orange (left vertical axis) and purple (right vertical axis) curves, respectively.

When several bulk flakes of $NbSe_2$ were freshly exfoliated and measured with SE from 1.15 eV to 6.22 eV, we obtain the curves shown in Figure 4 (b). The real component is shown in the top panel as an orange curve and agrees well the KKA counterpart (and will be described in more detail in the next subsection). The same observation holds true for the imaginary component in the middle panel. The dielectric function obtained with SE was then used to calculate an artificial DRC curve to compare with the original data. This comparison is shown in the bottom panel, along with a similarly generated DRC curve from KKA, which will be described later.

B. Kramers-Kronig Analysis on DRC Data

KKA was used to extract $\varepsilon(E)$ for bulk, 3L, 2L, and 1L $NbSe_2$ from their corresponding DRC measurements [61-64]. As noted before, a rough estimate of the absorption of the material can be calculated from the DRC using Equation 1. The absorption and ε_2 are related by $\frac{\varepsilon_2}{A(E)} = \frac{\hbar c}{EL}$, where E is the energy and L is the layer thickness [62]. This estimate provides an initial guess of ε_2 which subsequently undergoes an iterative process to optimize the accuracy of the dielectric

function extracted from DRC measurements, and whose procedure is well documented in [63]. This procedure also involves generating a DRC curve using the obtained dielectric function, and only until the generated and experimental DRC curves match to a certain degree of accuracy does one stop the iteration process [63]. With a known ε_2, KKA is performed using Equation 2:

$$\varepsilon_1(E) = 1 + \frac{1}{\pi}\int_{-\infty}^{\infty} \frac{\varepsilon_2(E')}{E'-E}\, dE' \tag{2}$$

This full procedure is first done for bulk $NbSe_2$ and yields the result shown in Figure 4 (b). The real (top panel) and imaginary (middle panel) components are presented as blue and green curves, respectively, within the measurement range. The minor disagreement between KKA-obtained $\varepsilon_{\text{bulk}}(E)$ and SE-obtained $\varepsilon_{\text{bulk}}(E)$ closer to the endpoints of the DRC energy range is a result of the assumption involved in KKA. It is assumed in Equation 2 that the optical behavior of the material for all energies is known. However, DRC measurements can only probe the photon energies between 1.15 eV and 3.5 eV. In our calculation, we artificially set the DRC data as approaching zero asymptotically. The expected error from this treatment is underestimating the spectral weight around the endpoint regions of ε_2. This underestimation is exactly what happens in the middle panel of Fig. 4 (b), where ε_2 begins to deviate from SE data after 3 eV.

In the bottom panel of Fig. 4 (b), the KKA-obtained $\varepsilon_{\text{bulk}}(E)$ is used to generate a DRC curve as a method of verifying the success of the calculation, and the obtained curve agrees well with the original DRC data. Due to the limitations of DRC, minor deviations are seen at the endpoints with the SE-generated DRC curve in yellow. Overall, KKA still provides a useful way of extracting $\varepsilon(E)$ over a range of energies, and since KKA agrees with a large portion of the SE-

obtained $\varepsilon_{\mathrm{bulk}}(E)$, KKA was utilized to obtain the dielectric function for the few-layer flakes as well.

The DRC curves were used to extract $\varepsilon(E)$ for each thickness, and the results are shown in Figure 4 (c). For the 1L case, there is a substantial change in the dielectric function compared with the gradual changes in thicker flakes' functions, most notably at energies below 2 eV. We attribute the decrease in the dielectric strength to the reduction of available electronic states in 1L $NbSe_2$, which has been previously explored experimentally and theoretically [44, 65]. Specifically, in 1L, a gap in electronic states was seen along both the Γ-K and Γ-M directions in the Brillouin zone with angle-resolved photoemission spectroscopy [44].

These functions also reveal some insight onto the observations made with Raman. Notice that an absorptive response in the bulk ε_2 is seen at approximately 2.5 eV, and as the layer number decrease, the absorption both asymptotically redshifts to 620 nm (2 eV) and increases in strength. Since ε_2 is the dominant factor in determining the actual absorption of the material, its behavior as a function of layer number is crucial in helping us understand the resonance Raman observations made in Figure 2 (b). For all thicknesses, more light is absorbed at shorter wavelength (< 500 nm) which may be the reason for the increased intensity of the E_{2g} with shorter wavelengths. Though this may clarify one of mechanisms by which the resonance Raman takes on a local maximum, it is not fully clear why the A_{1g} intensity increases relative to the E_{2g} for longer wavelengths when less light is absorbed. This secondary phenomenon may require further theoretical analyses.

V. CONCLUSIONS

In summary, we have performed a comprehensive optical examination of $NbSe_2$, both for the bulk crystal and its atomically thin layers. The Raman spectra were analyzed along with electrical transport to verify the quality of the superconducting material. Furthermore, the reflectance contrast was measured as a function of layer number, allowing for the extraction of $\varepsilon(E)$ for bulk, 3L, 2L, and 1L $NbSe_2$ by using Kramers-Kronig analysis. Spectroscopic ellipsometry was also performed to further support the accuracy of the extracted dielectric functions of $NbSe_2$.

ACKNOWLEDGMENTS AND NOTES

H.M.H. designed the experiment and collected and analyzed data. A.F.R. provided assistance with ellipsometry measurements. S.K. and A.V.D. provided crystals. J.T. assisted with electrical measurements. The manuscript was written through contributions of all authors. All authors have given approval to the final version of the manuscript. H.M.H. and A.F.R would like to thank the National Research Council's Research Associateship Program for the opportunity. S.K. acknowledges support from the U.S. Department of Commerce, National Institute of Standards and Technology under the financial assistance award 70NANB18H155 and would like to thank Theiss Research for the opportunity. The authors thank Amber McCreary and Thomas Germer for additional assistance. The authors declare no competing interest.

REFERENCES

[1] K. S. Novoselov, D. Jiang, F. Schedin, T. J. Booth, V. V. Khotkevich, S. V. Morozov, and A. K. Geim, Proc. Natl. Acad. Sci. USA **102**, 10451 (2005).

[2] S. Das, J. A. Robinson, M. Dubey, H. Terrones, and M. Terrones, Annu. Rev. Mater. Sci. **45**, 1 (2015).

[3] S. Z. Butler, S. M. Hollen, L. Cao, Y. Cui, J. A. Gupta, H. R. Gutiérrez, T. F. Heinz, S. S. Hong, J. Huang, A. F. Ismach, E. Johnston-Halperin, M. Kuno, V. V. Plashnitsa, R. D. Robinson, R. S. Ruoff, S. Salahuddin, J. Shan, L. Shi, M. G. Spencer, and M. Terrones, ACS Nano **7**, 2898 (2013).

[4] P. Tonndorf, R. Schmidt, P. Böttger, X. Zhang, J. Börner, A. Liebig, M. Albrecht, C. Kloc, O. Gordan, D. R. T. Zahn, S. M. de Vasconcellos, and R. Bratschitsch, Opt. Express **21**, 4908 (2013).

[5] K. F. Mak, C. Lee, J. Hone, J. Shan, and T. F. Heinz, Phys. Rev. Lett. **105**, 136805 (2010).

[6] M. Chhowalla, H. S. Shin, G. Eda, L. J. Li, K. P. Loh, and H. Zhang, Nat. Chem. **5**, 263 (2013).

[7] H. Li, G. Lu, Y. L. Wang, Z. Y. Yin, C. X. Cong, Q. Y. He, L. Wang, F. Ding, T. Yu, and H. Zhang, Small **9**, 1974 (2013).

[8] D. Y. Qiu, F. H. da Jornada, and S. G. Louie, Phys. Rev. Lett. **111**, 216805 (2013).

[9] T. C. Berkelbach, M. S. Hybertsen, and D. R. Reichman, Phys. Rev. B **88**, 045318 (2013).

[10] G. Moody, C. K. Dass, K. Hao, C.-H. Chen, L.-J. Li, A. Singh, K. Tran, G. Clark, X. Xu, G. Berghuser, E. Malic, A. Knorr, and X. Li, Nat. Commun. **6**, 8315 (2015).

[11] Q. Wang, K. Kalantar-Zadeh, A. Kis, J. N. Coleman, and M. S. Strano, Nat. Nanotechnol. **7**, 699 (2012).

[12] S. Manzeli, D. Ovchinnikov, D. Pasquier, O. V. Yazyev, and A. Kis, Nat. Rev. Mater. **2**, 17033 (2017).

[13] G. Wang, A. Chernikov, M. M. Glazov, T. F. Heinz, X. Marie, T. Amand, and B. Urbaszek, Rev. Mod. Phys. **90**, 021001 (2018).

[14] Y.-T. Hsu, A. Vaezi, M. H. Fischer, and E.-A. Kim, Nat. Commun. **8**, 14985 (2017).

[15] D. E. Moncton, J. D. Axe, and F. J. DiSalvo, Phys. Rev. B **16**, 801 (1977).

[16] G. Gruner, The dynamics of CDWs. Rev. Mod. Phys. **60**, 1129 (1988).

[17] M. D. Johannes and I. I. Mazin, Phys. Rev. B **77**, 165135 (2008).

[18] F. Weber, S. Rosenkranz, J.-P. Castellan, R. Osborn, R. Hott, R. Heid, K.-P. Bohnen, T. Egami, A. H. Said, and D. Reznik, Phys. Rev. Lett. **107**, 107403 (2011).

[19] C. J. Arguello, S. P. Chockalingam, E. P. Rosenthal, L. Zhao, C. Gutierrez, J. H. Kang, W. C. Chung, R. M. Fernandes, S. Jia, A. J. Millis, R. J. Cava, and A. N. Pasupathy, Phys. Rev. B **89**, 235115 (2014).

[20] U. Chatterjee, J. Zhao, M. Iavarone, R. Di Capua, J.P. Castellan, G. Karapetrov, C.D. Malliakas, M.G. Kanatzidis, H. Claus, J.P.C. Ruff, F. Weber, J. vanWezel, J.C. Campuzano, R. Osborn, M. Randeria, N. Trivedi, M.R. Norman, and S. Rosenkranz, Nat. Commun. **6**, 6313 (2014).

[21] X. Xi, L. Zhao, Z. Wang, H. Berger, L. Forro, J. Shan, and K. F. Mak, Nat. Nanotechnol. **10**, 765 (2015).

[22] X. Xi, H. Berger, L. Forro, J. Shan, and K. F. Mak, Phys. Rev. Lett. **117**, 106801 (2016).

[23] H. Suderow, V. G. Tissen, J. P. Brison, J. L. Martinez, and S. Vieira, Phys. Rev. Lett. **95**, 117006 (2005).

[24] M. S El-Bana, D. Wolverson, S. Russo, G. Balakrishnan, D. M. Paul, and S. J. Bending, Supercond. Sci. Technol. **26**, 125020 (2013).

[25] N. F. Q. Yuan, K. F. Mak, and K. T. Law, Phys. Rev. Lett. **113**, 097001 (2014).

[26] X. Zhu, Y. Guo, H. Cheng, J. Dai, X. An, J. Zhao, K. Tian, S. Wei, X. C. Zeng, C. Wu, and Y. Xie, Nat. Commun. **7**, 11210 (2016).

[27] C.-S. Lian, C. Si, and W. Duan, Nano Lett. **18**, 2924 (2018).

[28] Y. Zhou, Z. Wang, P. Yang, X. Zu, L. Yang, X. Sun, and F. Gao, ACS Nano **6**, 9727 (2012).

[29] F. Flicker and J. van Wezel, Nat. Commun. **6**, 7034 (2015).

[30] X. Xi, Z. Wang, W. Zhao, J.-H. Park, K. T. Law, H. Berger, L. F., J. Shan and K. F. Mak, Nat. Phys. **12**, 139 (2016).

[31] L. Bawden, S.P. Cooil, F. Mazzola, J.M. Riley, L.J. Collins-McIntyre, V. Sunko, K. W. B. Hunvik, M. Leandersson, C.M. Polley, T. Balasubramanian, T.K. Kim, M. Hoesch, J.W. Wells, G. Balakrishnan, M.S. Bahramy and P.D.C. King, Nat. Commun. **7**, 11711 (2016).

[32] J. F. Scott, Rev. Mod. Phys. **46**, 83 (1974).

[33] D. J. Rahn, S. Hellmann, M. Kallane, C. Sohrt, T. K. Kim, L. Kipp, and K. Rossnagel, Phys. Rev. B **85**, 224532 (2012).

[34] Y. Noat, J. A. Silva-Guillen, T. Cren, V. Cherkez, C. Brun, S. Pons, F. Debontridder, D. Roditchev, W. Sacks, L. Cario, P. Ordejon, A. Garcıa, and E. Canadell, Phys. Rev. B **92**, 134510 (2015).

[35] F. Bischoff, W. Auwarter, J.V. Barth, A. Schiffrin, M. Fuhrer, and B. Weber, Chem. Mater. **29**, 9907 (2017).

[36] C.-Z. Xu, X. Wang, P. Chen, D. Flototto, J. A. Hlevyack, M.-K. Lin, G. Bian, S.-K. Mo, and T.-C. Chiang, Phys. Rev. Mater. **2**, 064002 (2018).

[37] M.A. Measson, Y. Gallais, M. Cazayous, B. Clair, P. Rodiere, L. Cario, and A. Sacuto, Phys. Rev. B **89**, 060503(R) (2014).

[38] A. Mialitsin, J. Phys. Chem. Solids **72**, 568 (2011).

[39] S.V. Dordevic, D.N. Basov, R.C. Dynes, B. Ruzicka, V. Vescoli, L. Degiorgi, H. Berger, R. Gaal, L. Forro, and E. Bucher, Eur. Phys. J. B **33**, 15 (2003).

[40] G.E. Meyers and G.L. Montet, J. Appl. Phys. **41**, 4642 (1970).

[41] Y. Cao, A. Mishchenko, G. L. Yu, E. Khestanova, A. P. Rooney, E. Prestat, A. V. Kretinin, P. Blake, M. B. Shalom, C. Woods, J. Chapman, G. Balakrishnan, I. V. Grigorieva, K. S. Novoselov, B. A. Piot, M. Potemski, K. Watanabe, T. Taniguchi, S. J. Haigh, A. K. Geim, and R. V. Gorbachev, Nano Lett. **15**, 4914 (2015).

[42] A. W. Tsen, B. Hunt, Y. D. Kim, Z. J. Yuan, S. Jia, R. J. Cava, J. Hone, P. Kim, C. R. Dean and A. N. Pasupathy, Nat. Phys. **12**, 208 (2016).

[43] R. He, J. van Baren, J.-A. Yan, X. Xi, Z. Ye, G. Ye, I.-H. Lu, S.M. Leong, and C.H. Lui, 2D Mater. **3**, 031008 (2016).

[44] M. M. Ugeda, A. J. Bradley, Y. Zhang, S. Onishi, Y. Chen, W. Ruan, C. Ojeda-Aristizabal, H. Ryu, M. T. Edmonds, H.-Z. Tsai, A. Riss, S.-K. Mo, D. Lee, A. Zettl, Z. Hussain, Z.-X. Shen and M. F. Crommie, Nat. Phys. **12**, 92 (2016).

[45] E. Sohn, X. Xi, W.-Y. He, S. Jiang, Z. Wang, K. Kang, J.-H. Park, H. Berger, L. Forro, K. T. Law, J. Shan, and K. F. Mak, Nat. Mater. **17**, 504 (2018).

[46] P. Cudazzo, M. Gatti, and A. Rubio, New J. Phys. **15**, 125005 (2013).

[47] J. C. Tsang, J. E. Smith, Jr., and M. W. Shafer, Phys. Rev. Lett. **37**, 1407 (1976).

[48] Y. Wu, M. An, R. Xiong, J. Shi, and Q. M. Zhang, J. Phys. D: Appl. Phys. **41**, 175408 (2008).

[49] X. Zhang, Q.-H. Tan, J.-B. Wu, W. Shi, and P.-H. Tan, Nanoscale. **8**, 6435 (2016).

[50] E. del Corro, H. Terrones, A. Elias, C. Fantini, S. Feng, M. A. Nguyen, T. E. Mallouk, M. Terrones, and M. A. Pimenta, ACS Nano **8**, 9629 (2014).

[51] E. del Corro, A. Botello-Méndez, Y. Gillet, A. L. Elias, H. Terrones, S. Feng, C. Fantini, D. Rhodes, N. Pradhan, L. Balicas, X. Gonze, J.-C. Charlier, M. Terrones, and M. A. Pimenta, Nano Lett. **16**, 2363 (2016).

[52] J. U. Lee, J. Park, Y.-W. Son, and H. Cheong, RR in MoS2. Nanoscale **7**, 3329 (2015).

[53] M. R. Molas, K. Nogajewski, M. Potemski, and A. Babinski, Sci. Rep. **7**, 5036 (2017).

[54] D. Nam, J.-U. Lee, and H. Cheong, Sci. Rep. **5**, 17113 (2015).

[55] B. R. Carvalho, L. M. Malard, J. M. Alves, C. Fantini, and M. A. Pimenta, Phys. Rev. Lett. **114**, 136403 (2015).

[56] P. Soubelet, A. E. Bruchhausen, A. Fainstein, K. Nogajewski, and C. Faugeras, Phys. Rev. B **93**, 155407 (2016).

[57] Commercial equipment, instruments, and materials are identified in this paper in order to specify the experimental procedure adequately. Such identification is not intended to imply recommendation or endorsement by the National Institute of Standards and Technology or the United States government, nor is it intended to imply that the materials or equipment identified are necessarily the best available for the purpose.

[58] J. C. Tsang, J. E. Smith, Jr., and M. W. Shafer, Solid State Commun. **27**, 145 (1978).

[59] See Supplemental Material at [URL] for comparisons of the CVT-grown and commercial crystal, soft Raman mode data, polarization-dependent measurements, and details on the oxidation effects on $NbSe_2$. This material includes Ref. [66].

[60] A. F. Rigosi, H. M. Hill, Y. L. Li, A. Chernikov, and T. F. Heinz, Nano Lett. **15**, 5033 (2015).

[61] Y. Li, A. Chernikov, X. Zhang, A. Rigosi, H. M. Hill, A. M. van der Zande, D. A. Chenet, E.-M. Shih, J. Hone, and T. F. Heinz, Phys. Rev. B **90**, 205422 (2014).

[62] D. Kecik, C. Bacaksiz, R. T. Senger, and E. Durgun, Phys. Rev. B **92**, 165408 (2015).

[63] H. M. Hill, A. F. Rigosi, S. Chowdhury, Y. Yang, N. V. Nguyen, F. Tavazza, R. E. Elmquist, D. B. Newell, and A. R. Hight Walker, Phys. Rev. B **96**, 195437 (2017).

[64] A. F. Rigosi, H. M. Hill, N. R. Glavin, S. J. Pookpanratana, Y. Yang, A. G. Boosalis, J. Hu, A. Rice, A. A. Allerman, N. Nguyen, C. A. Hacker, R. E. Elmquist, A. R. Hight Walker, D. B. Newell, 2D Mater. **5**, 011011 (2018).

[65] M. Calandra, I. I. Mazin, and F. Mauri, Phys. Rev. B **80**, 241108(R) (2009).

[66] Y. Zhao, Z. Zhang, and Y. Lin, J. Phys. D: Appl. Phys. **37**, 3392 (2004).

TABLE OF CONTENTS GRAPHIC (END OF DOC)